Nanoscale

ROYAL SOCIETY OF CHEMISTRY

PAPER

View Article Online
View Journal | View Issue



Cite this: *Nanoscale*, 2020, **12**, 24146

# An all-in-one theranostic nanoplatform based on upconversion dendritic mesoporous silica nanocomposites for synergistic chemodynamic/photodynamic/gas therapy†

Shikai Liu,[a] Wenting Li,[a] Shuming Dong,[a] Fangmei Zhang,[a] Yushan Dong,[a] Boshi Tian,[a] Fei He,*[a] Shili Gai*[a] and Piaoping Yang *[a,b]

Gasotransmitters with high therapeutic efficacy and biosafety have been drawing the attention of researchers. Nevertheless, how to effectively deliver gases to and precisely control their generation at the lesion as well as integrate them with other therapies to realize precision therapy have remained elusive. Herein, we report a versatile $Cu^{2+}$-initiated nitric oxide (NO) nanocomposite for multimodal imaging-guided synergistic chemodynamic/photodynamic/gas therapy. After the nanomedicine was ingested by tumor cells, the acidic tumor microenvironment accelerated the decomposition of $CuO_2$ and simultaneously triggered the Fenton-like catalytic reaction of $Cu^{2+}$ and $H_2O_2$ to produce highly toxic $^{\bullet}OH$. By virtue of the NO generation and glutathione depletion, UMNOCC-PEG can relieve the antioxidant capacity and hypoxia of the tumor to improve the efficiency of chemodynamic therapy (CDT) and photodynamic therapy (PDT). Importantly, NO and reactive oxygen species (ROS) can generate reactive nitrogen species (RNS), which can result in DNA damage, further improving the therapeutic effect (cell apoptosis rate up to 93.4%). Moreover, the inherent properties of lanthanide ions endow UMNOCC-PEG with upconversion luminescence (UCL), CT and MRI trimodal imaging capability, achieving precise cancer treatment. By taking advantage of these features, the strategy developed here may provide a promising application foreground to conquer malignant tumors.

Received 21st September 2020,
Accepted 12th November 2020

DOI: 10.1039/d0nr06790c

rsc.li/nanoscale



## Introduction

As a "green" strategy for cancer treatment, the emerging gas therapy has aroused increasing interest due to strong physiological modulation functions and negligible side effects.[1–3] Among the gasotransmitter family, nitric oxide (NO) is one of the most noteworthy physiological messenger agents, being indispensable in angiogenesis, cell apoptosis, immune responses, neurotransmission and cardiovascular homeostasis.[4–6] Specifically in cancer treatment, NO not only kills cancer cells efficiently in a relatively high concentration range (>1 μM) *via* the oxidation or nitrosation of mitochondria and DNA, but also successfully enhances the efficacy of chemotherapy or PDT.[7–9] Of particular interest, NO molecules have a variety of metabolic pathways, which totally compensate for the leakage of drugs and unnecessary cytotoxicity caused to normal cells.[10,11] Nevertheless, the extremely short half-life and poor stability of the NO donor severely hinder the development of NO-based therapeutic agents for practical applications.[12,13] Hence, developing smart delivery nanocarriers containing biocompatible and activatable NO donors, which can be stimulated by external or endogenous substances to induce the release of NO, is still a great challenge.

With this end in view, many research efforts have been made to develop a variety of stimulus-responsive NO delivery systems. In the design of the stimulus-responsive nanoplatform for NO release, the donor and trigger are two vital factors. Until now, s-nitrosothiol (RSNO)-based NO delivery nanocarriers have been generally preferred as a major NO donor due to their advantage of excellent biocompatibility.[14–16] RSNO can release NO when triggered by a series of stimuli, such as ultraviolet light, heat, X-ray, and certain metal ions ($Cu^{2+}$, $Hg^{2+}$, *etc.*). Among these triggers, light and heat have the characteristics of shallow penetration and poor controllability, respectively, and X-ray may have strong ionizing radiation on the normal organs.[17,18] In addition, mercury ions are

[a]*Key Laboratory of Superlight Materials and Surface Technology, Ministry of Education, College of Materials Science and Chemical Engineering, Harbin Engineering University, Harbin, 150001, P. R. China.*
*E-mail: hefei@hrbeu.edu.cn, gaishili@hrbeu.edu.cn, yangpiaoping@hrbeu.edu.cn*
[b]*College of Sciences, Heihe University, 164300, P. R. China*

†Electronic supplementary information (ESI) available. See DOI: 10.1039/d0nr06790c

highly toxic to organisms. All of these restrictions severely impede their potential applications toward clinical treatment. Fortunately, previous works have demonstrated that $Cu^{2+}$ can induce RNO to release NO. Therefore, combining RSNO with copper-containing materials is expected to generate tumor microenvironment (TME)-responsive NO release for cancer treatment.

ROS, including singlet oxygen ($^1O_2$), superoxide anions ($^{\bullet}O^{2-}$) and hydroxyl radicals ($^{\bullet}OH$), have been considered as important therapeutic agents for tumor, which can induce cellular necrosis or apoptosis when their levels exceed the threshold.[19–24] Among the three types of ROS, $^{\bullet}OH$ is a hypertoxic and nonselective oxidant, which can damage almost all types of organic molecules, including DNA, amino/nucleic acids, proteins, and lipids.[25–27] $^1O_2$ is the main mediator of photocytotoxicity, which can irreversibly destroy the treated biological tissues and cause the oxidation and degradation of the biofilm.[28,29] Therefore, the rational design of multifunctional nanoplatforms integrated with $^{\bullet}OH$ and $^1O_2$ provides a broad prospect for efficient ROS-mediated tumor therapy.[30]

As an emerging cancer treatment strategy, PDT has shown many advantages over other traditional therapies, such as low side effects, minimal invasiveness, and high applicability. Nevertheless, the therapeutic effect of PDT is limited by the poor $^1O_2$ generation efficiency, which causes hypoxia and the overproduction of glutathione (GSH) in the TME.[31–35] Hypoxia is a prominent feature of solid tumors, and principally results from the insufficient blood supply to cancer tissues and the excessive tumor cell growth. Moreover, high level of intracellular GSH serves as a natural oxidant scavenger, protecting cancer cells from ROS damage. Coincidently, NO can induce the relaxation of smooth muscle cells and increase the blood flow, and is clinically used to improve the oxygen supply in patients with myocardial infarction. Thus, the development of NO-based delivery nanocarriers which relieve tumor hypoxia characteristics will significantly enhance the PDT effect.[36,37] On the other hand, CDT is a new therapeutic approach that depends on Fenton reactions to produce oxidative $^{\bullet}OH$, the most toxic ROS.[38–40] In the past few years, a variety of nanoparticles have been employed as Fenton catalyst donors to catalyze endogenous $H_2O_2$.[41–43] Although many types of cancer cells exhibit higher levels of intracellular hydrogen peroxide than normal cells, the CDT efficacy is still not satisfactory by catalyzing endogenous hydrogen peroxide. Therefore, the introduction of self-supplying $H_2O_2$ into CDT agents is an effective strategy to improve their anticancer efficiency.[44,45]

In this demonstration, we constructed a multifunctional nanotheranostic system with dendritic porous silica based on upconversion nanoparticles (UCNPs) for UCL/MRI/CT trimodal bioimaging guided synergistic CDT/PDT/gas therapy. In brief, using a bicontinuous microemulsion reaction system, a mesoporous silica layer is uniformly coated onto the surface of UCNPs, which increased the loading of the NO donor and improved the biocompatibility of nanoparticles despite the poor biocompatibility of upconversion nanoparticles. Subsequently, copper peroxide nanodots, chlorin e6 (Ce6) and polyethylene glycol (PEG) are loaded into silicon pores to obtain UCNPs@dMSN-SNO@$CuO_2$-Ce6-PEG (UMNOCC-PEG, Scheme 1a). After endocytosis by cancer cells, copper peroxide nanodots are decomposed in the acidic TME, allowing the release of a large number of copper ions and abundant $H_2O_2$ to achieve efficient CDT and considerable NO-releasing performance. Significantly, such a TME-responsive NO-releasing nanoreactor enables hypoxia relief and GSH depletion, thereby enhancing the efficacy of PDT. Importantly, the simultaneous release of ROS and NO ensures the efficient generation of RNS, which can directly induce DNA damage by triggering free radical peroxidation. Moreover, due to the unique properties of rare earth ions, the developed nanoplatform possesses excellent tri-mode imaging (UCL, CT and MRI) capability, which is conducive to monitor the whole treatment process in real time.

## Results and discussion

### Synthesis and characterization of UMNOCC-PEG

Herein, a simple approach was used to prepare dendritic porous silica-coated UMNOCC-PEG, which was used as a TME-responsive Fenton-like and upconversion-mediated NO donor to achieve CDT/PDT/gas combinatorial therapy under UCL, MRI and CT imaging guidance. The tumor theranostic application and therapeutic mechanism of UMNOCC-PEG are illustrated in Scheme 1b and c. Firstly, after ingestion by tumor cells, copper peroxide nanodots were decomposed into $Cu^{2+}$ and $H_2O_2$ in the acidic TME. The overexpression of GSH in tumor cells reduced $Cu^{2+}$ to $Cu^{+}$, which further catalyzed $H_2O_2$ to achieve satisfactory CDT. Secondly, the RSNO decomposition reaction begins by tracing the thiolate anion through $Cu^{2+}$ to produce $Cu^{+}$, and the RSNO compounds were then reduced to initiate NO release by $Cu^{+}$.[46,47] When UMNOCC-PEG is exposed to near-infrared (NIR) light, UCNPs are introduced as energy sensors to convert NIR light into visible light *in situ*, and further awaken the photosensitizer (Ce6) to produce singlet oxygen. Notably, NO can relieve hypoxia in tumor tissues by relaxing the smooth muscle cells and speeding up the blood flow, thereby improving the efficiency of PDT. Finally, NO reacts with ROS to produce the RNS, which can result in DNA damage and further improve the efficacy of cancer treatment. Monodispersed β-$NaGdF_4$:20%Yb,2%Er UCNPs with a particle size of about 28 nm were fabricated by a high-temperature decomposition method, and the transmission electron microscope (TEM) images are shown in Fig. 1a and S1a.† Subsequently, UCNP@dMSN was prepared in a heterogeneous oil–water microemulsion phase. The microemulsion method allows the surfactants and reactants to self-assemble in the interface.[48–50] After surfactant removal, the large internal surfaces and pores of the silica shell were coated onto the surface of the UCNPs. Afterwards, silicon hydroxyl (Si–OH) was functionalized with sulfhydryl (SH) groups and further nitrated with *tert*-butyl nitrite to obtain UCNP@dMSN-SNO (named UMNO). The TEM

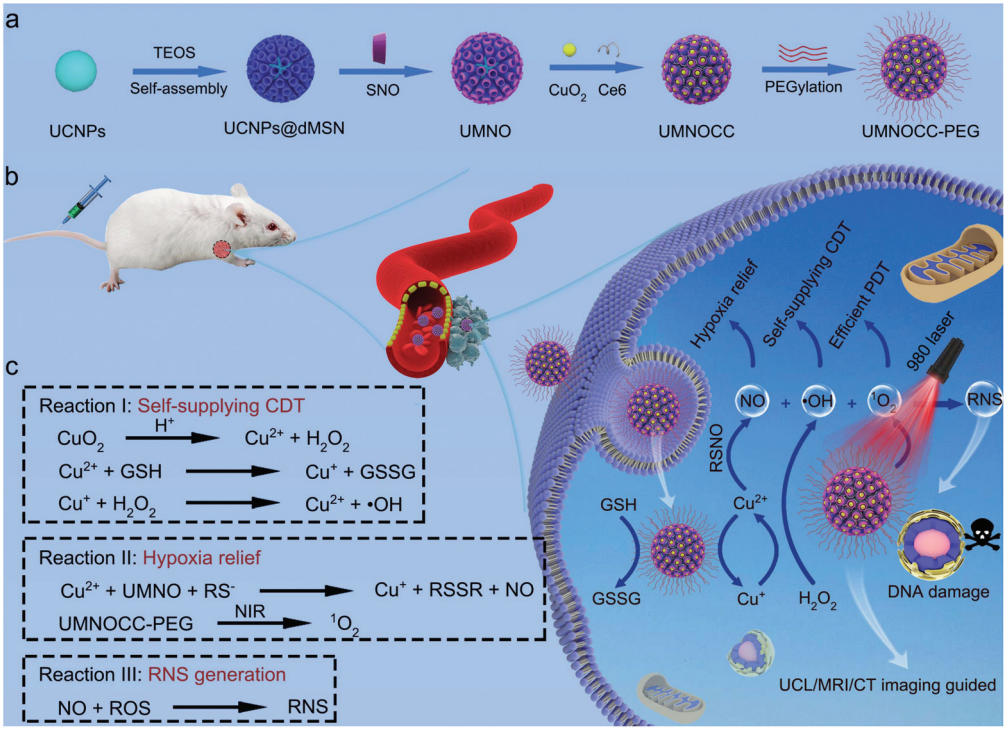


**Scheme 1** (a) Schematic illustration for the synthesis of UMNOCC-PEG. (b) Scheme of the tumor theranostic application and (c) therapeutic mechanism of UMNOCC-PEG for the improvement of PDT induced by NIR, $Cu^{2+}$-initiated CDT and gas therapy.

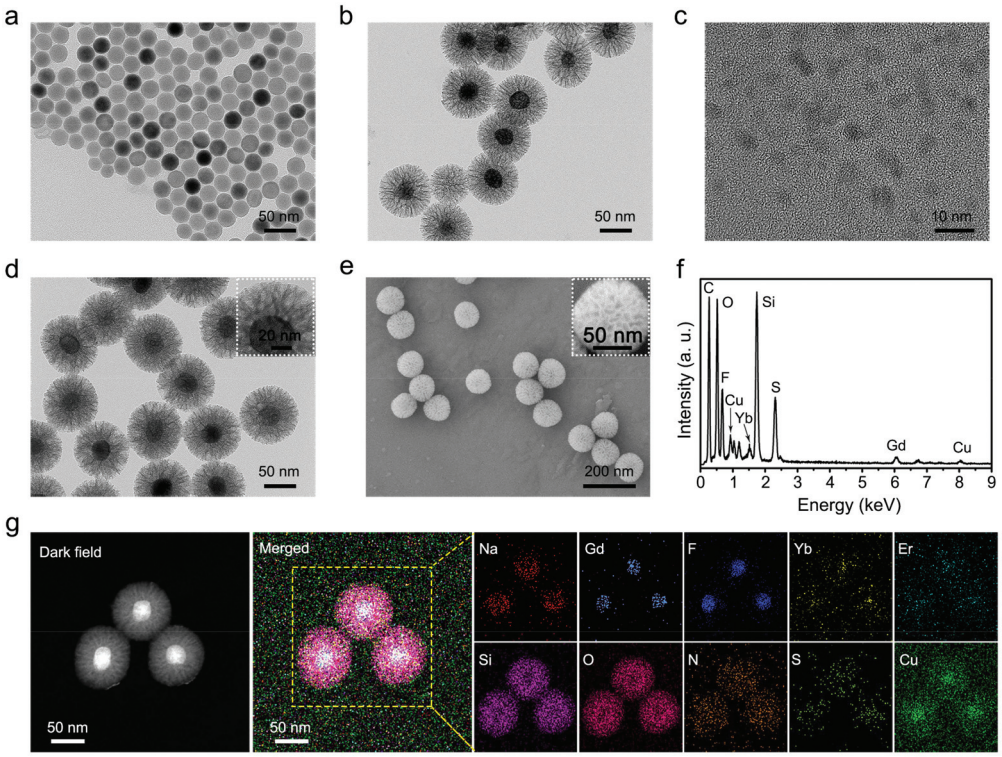


**Fig. 1** Structural and compositional characterization of UMNOCC-PEG nanoparticles. TEM images of (a) the $NaGdF_4$:Yb,Er core nanoparticles, (b) UCNP@dMSN-SNO, (c) $CuO_2$ nanodots, and (d) UMNOCC-PEG nanoparticles. (e) SEM image and (f) corresponding EDS spectrum of the UMNOCC-PEG nanoparticles. (g) Dark-field STEM image and the corresponding elemental mappings of UMNOCC-PEG nanoparticles.

image showed the uniform dendritic mesoporous silica layer coated on the surface of the UCNPs, and the average size of UMNO increased to 106 nm (Fig. 1b). In addition, the energy-dispersive spectrum of UMNO showed that the sample was mainly composed of Si, Gd, Yb, Na, F, and Er, showing the existence of the silica shell, as shown in Fig. S2.† In order to obtain the $Cu^{2+}$-controlled NO-release nanoplatform, $CuO_2$ was prepared by the reaction of $H_2O_2$, NaOH, and $CuCl_2$ containing PVP for 0.5 h. As can be seen in Fig. 1c and S1b,† the prepared $CuO_2$ nanodots showed a relatively uniform size of approximately 5 nm and excellent dispersibility. Ultimately, UMNOCC-PEG was obtained by integrating Ce6 and $CuO_2$, and then modified with PEG. The unique core–shell structure and dendritic shape were well preserved without obvious deformation (Fig. 1d). The most typical characteristics of the mesoporous structure are the porous channel and surface morphology, which are observed in the scanning electron microscope (SEM) image (Fig. 1e). In addition, all the major elements, namely Cu, S, Si, N, Na, Gd, F, O, Yb, and Er, are shown in the energy-dispersive spectroscopy (EDS) spectrum (Fig. 1f) and corresponding elemental mapping (Fig. 1g). All the above results confirmed that UMNOCC-PEG has been successfully constructed.

The Brunauer–Emmett–Teller (BET) surface area and corresponding pore size distribution of UCNPs@dMSN are shown in Fig. 2a and b. UCNPs@dMSN possessed a relatively high surface area of 194.05 $m^2\ g^{-1}$ and a pore size of 26.6 nm, which provided sufficient space for the efficient loading of $CuO_2$ and Ce6 molecules.[51] Notably, the specific surface area and corresponding pore diameter distribution of UMNOCC-PEG were decreased to 81.5 $m^2\ g^{-1}$ and 9.5 nm (Fig. S3†), respectively, suggesting that the $CuO_2$ and Ce6 molecules were successfully loaded into the pores of silica. The X-ray diffraction (XRD) patterns of the UCNPs, UMNO, and UMNOCC-PEG are displayed in Fig. 2c. The pattern of the UCNPs was identical with the encoding of hexagonal phase $NaGdF_4$ (JCPDS no. 27-0699), confirming the successful preparation of $NaGdF_4$-based luminescent nanoparticles. The broad band peak of UMNO at $2\theta$ of 22° was assigned to the dendritic mesoporous silica shell. The spectra of UMNOCC-PEG revealed a sharp and strong peak around 20°, which was consistent with the reported literature for $CuO_2$.[52] Subsequently, the chemical composition and element state of UMNOCC-PEG were investigated by X-ray photoelectron spectroscopy (XPS). The XPS survey spectrum of UMNOCC-PEG showed the existence of Cu, O, Si, and C, which

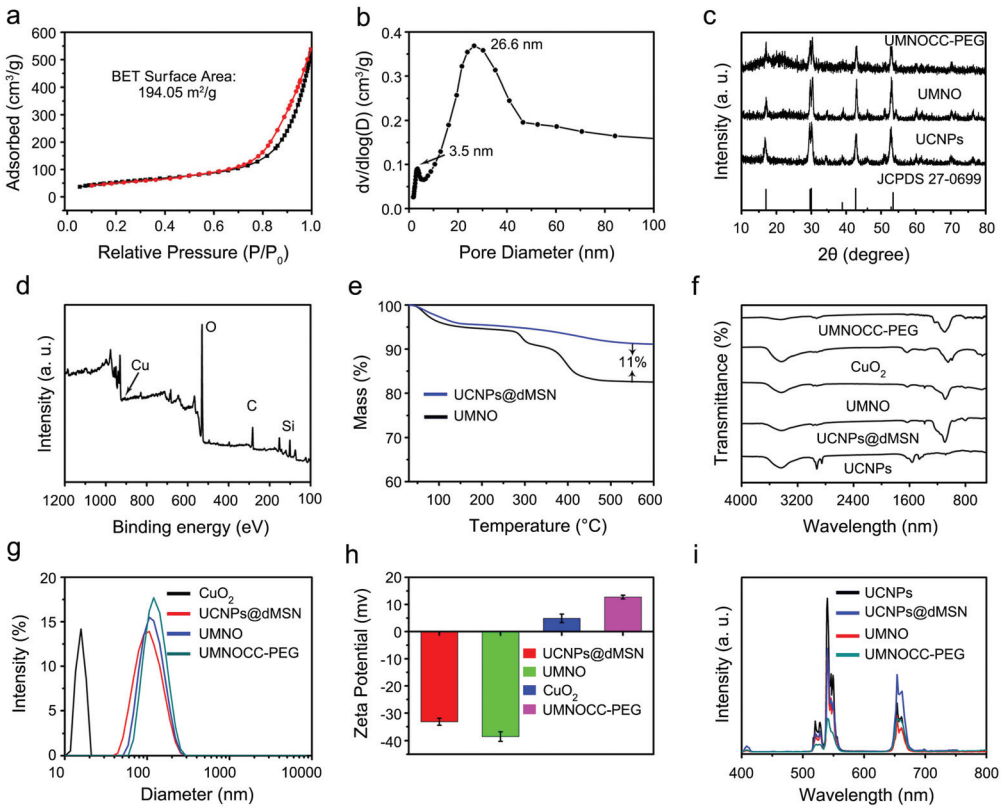


**Fig. 2** Characterization of UMNOCC-PEG nanoparticles. (a) $N_2$ absorption-desorption isotherms and (b) corresponding pore-size distribution of UCSP@dMSN. (c) XRD patterns of UCNPs, UMNO, and UMNOCC-PEG. (d) Survey XPS spectra of UMNOCC-PEG and (e) thermogravimetric analysis curves of UCNPs@dMSN and UMNO. (f) FT-IR spectra of UCNPs, UCNPs@dMSN, UMNO, $CuO_2$, and UMNOCC-PEG. (g) Particle-size distribution of $CuO_2$, UCNPs@dMSN, UMNO, and UMNOCC-PEG. (h) Zeta potential of UCNPs@dMSN, UMNO, $CuO_2$, and UMNOCC-PEG. (i) Upconversion emission spectra of UCNPs, UCNPs@dMSN, UMNO, and UMNOCC-PEG.

was basically in agreement with the elemental mapping images (Fig. 2d). Furthermore, the high-resolution spectra of O 1s and Cu 2p are shown in Fig. S4a and b.† As shown in the O 1s high-resolution spectrum, the two peaks detected at 533.1 and 531.5 eV were attributed to O–O and C═O, separately, indicating the presence of peroxo groups and PVP.[53] In addition, the existence of peroxo groups in UMNOCC-PEG was determined by potassium permanganate colorimetry. As presented in Fig. S5,† the purple colour of potassium permanganate ($MnO_4^-$) disappeared as the concentration of UMNOCC-PEG increased, which was caused by the reduction of purple $MnO_4^-$ to colorless $Mn^{2+}$ by the peroxo groups. Then, the Cu 2p high-resolution spectrum showed two major characteristic peaks at 953.5 and 933.5 eV along with two satellite peaks at 962.1 and 942.1 eV, separately, which clearly indicated the presence of $Cu^{2+}$ ions. Thereafter, thermogravimetric analysis was employed to assess the loading capacity of the NO donor (Fig. 2e), in which the loading amount of UMNO was up to 11%, ensuring the potential high efficiency of gas therapy. The FT-IR spectra of each step are displayed in Fig. 2f; the UCNPs showed two broad bands at 1557 and 1467 $cm^{-1}$ which can be associated with the modified oleic acid groups. After coating the dendritic silica shell, the stretching vibration of the –OH groups was obvious at 947 and 3432 $cm^{-1}$. In addition, some characteristic bands were detected at 463 cm and 797 $cm^{-1}$, and were associated with the deformation vibrations and asymmetric stretching of the Si–O–Si bonds. For UMNO, two main peaks at 723 and 1467 $cm^{-1}$ were attributed to –S–N = and –N═O, separately, which confirmed the successful conjugation of –SNO into UMNO. In the $CuO_2$ spectrum, the band at around 1635 $cm^{-1}$ was assigned to the stretching vibration of C═O, further demonstrating the presence of PVP. UMNOCC-PEG showed a similar spectrum to that of UMNO due to the same functional groups.

Dynamic light scattering (DLS) was employed to determine the mean diameter of $CuO_2$, UCNPs@dMSN, UMNO, and UMNOCC-PEG, which was around 15.7, 106, 110, and 125 nm, respectively (Fig. 2g). The increased sizes were mainly due to the conjugation of the NO donor and the insertion of copper peroxide. In addition, the hydrodynamic diameter of UMNOCC-PEG in different solutions (culture medium, PBS and water) was about 125 nm as determined by DLS (Fig. S6a†), suggesting excellent dispersibility. Then, the UMNOCC-PEG nanoparticles were dispersed and oscillated in the above solution at different times. The particle diameter of UMNOCC-PEG in different solutions had little change, demonstrating that the UMNOCC-PEG nanoparticles had good stability in systems simulating a biological environment (Fig. S6b†). The subsequent zeta potential changes of UCNPs@dMSN, UMNO, $CuO_2$, and UMNOCC-PEG are shown in Fig. 2h. For UCNPs@dMSN, the surface potential showed a negative value, since the surface of UCNPs was coated with mesoporous silica. After modifying the NO donor, the surface potential of UMNO reduced from −33.2 to −38.5 mV, which was caused by the negative NO donor, and such surface potential changes further indicated that the NO donor was successfully loaded onto the surface of UCNPs@dMSN. After embedding copper peroxide with positive potential, the surface potential of UMNOCC-PEG increased to 12.7 mV, confirming the effective loading of $CuO_2$. The UCL spectra of the UCNPs, UCNPs@dMSN, UMNO, and UMNOCC-PEG are presented in Fig. 2i. The UCNPs show considerable upconversion emission around 650 nm, implying their potential to convert NIR light into visible light. After being irradiated with NIR light, three main emission peaks of $Er^{3+}$ at 510–530 nm ($^2H_{11/2} \rightarrow {}^4I_{15/2}$), 530–570 nm ($^4S_{3/2} \rightarrow {}^4I_{15/2}$) and 630–680 nm ($^4F_{9/2} \rightarrow {}^4I_{15/2}$) were clearly observed in the UCNP spectra. For UCNPs@dMSN, the emission intensity was significantly reduced because of the quenching effect of the silica shell. Compared with that of UCNPs@dMSN, the total peak intensity of UMNO decreased significantly, despite the quenching effect of the NO donor. As for UMNOCC-PEG, the emission attenuation was more serious in the red range due to the main absorption of the loaded Ce6, while the upconversion emission in aqueous solutions was stable at different time periods as shown in Fig. S7.† Subsequently, according to the UV–vis absorption spectra and the standard curve of Ce6, the loading capacity of Ce6 was calculated to be 23.4% (Fig. S8a and b†).

### Determination of ROS generation ability

Fig. 3a displays the upconversion emission spectra of UMNOCC-PEG and UV–vis absorption spectrum of Ce6. Obviously, the red emission region of UMNOCC-PEG overlaps with the absorption spectrum of Ce6 at 654 nm, suggesting that UMNOCC-PEG-emitted red light can activate the photosensitizers to realize photodynamic therapy. Thereafter, the capacity of extracellular singlet oxygen production was investigated using a 1,3-diphenylisobenzofuran (DPBF) chemical probe. When DPBF reacted with singlet oxygen generated from UMNOCC-PEG under NIR irradiation, the absorption intensity of DPBF at 425 nm decreased gradually (Fig. 3b). In contrast, there was no significant change in the control group after NIR radiation (Fig. 3c), suggesting that singlet oxygen was mainly generated by UMNOCC-PEG rather than NIR light.

Considering the decomposition of $CuO_2$ into $Cu^{2+}$ and $H_2O_2$ under a weak acid environment, UMNOCC-PEG may possess a satisfactory Fenton-like effect. Initially, the GSH consuming capacity of UMNOCC-PEG was evaluated using the UV–vis absorption spectra. DTNB, a –SH indicator probe, was introduced to detect the levels of GSH. With an increase of the reaction time, the absorbance at 410 nm decreased significantly, suggesting the depletion of GSH in the presence of UMNOCC-PEG (Fig. S9†). Subsequently, methylene blue (MB), a common chemical dye, was utilized to evaluate the performance of extracellular $^{\bullet}OH$ generation. In Fig. 3d, the absorption intensity of MB decreased gradually when the UMNOCC-PEG solution was mixed under an acid environment (pH = 6.5, 1 mM GSH) for 60 min. In comparison, no significant decrease could be detected under neutral conditions (pH = 7.4, 1 mM GSH), indicating that $CuO_2$ had excellent stability in a neutral environment (Fig. 3e). In addition, the absorption intensity of MB decreased slightly when the UMNOCC-PEG solution was

 

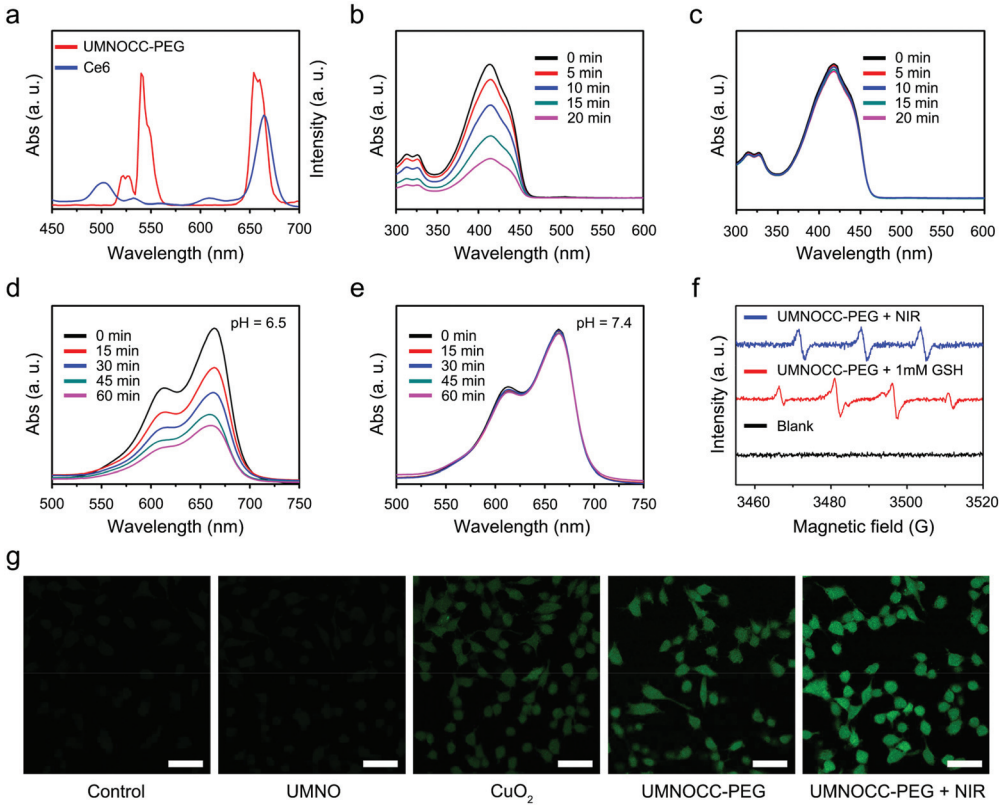


**Fig. 3** Determination of ROS generation ability. (a) Upconversion emission spectra of UMNOCC-PEG, and the UV–vis absorption spectra of Ce6 molecules. Absorbance spectra of DPBF treated (b) with and (c) without UMNOCC-PEG upon NIR laser irradiation. Time-dependent UV–vis absorption spectra of the MB contained UMNOCC-PEG solution in the presence of GSH (1 mM) at pH 6.5 (d) or 7.4 (e), respectively. (f) ESR spectra for the detection of ROS in the presence of TEMP and DMPO in aqueous solution. (g) CLSM images of HeLa cells for the detection of intracellular ROS under different treatments. Scale bar: 50 μm.

mixed under an acid environment (pH = 6.5, 0 mM GSH) for 60 min, suggesting a small amount of hydroxyl radical generation, since the resulting $H_2O_2$ reduced some of the $Cu^{2+}$ to $Cu^{+}$ (Fig. S10a†). Comparatively, no significant change in the absorption peak was detected in the control group (Fig. S10b†). The above results confirmed the acidity-sensitive generation of $^{\bullet}OH$ under catalysis by UMNOCC-PEG. In addition, we compared the $^{\bullet}OH$ production ability of UMNOCC-PEG and UMNOCC-PEG + bovine serum albumin (BSA) groups to determine whether the complex of proteins and $Cu^{2+}$ had an effect on CDT. The Fenton-like reaction process was investigated using the 3,3′,5,5′-tetramethylbenzidine (TMB) assay which can oxidize the colorless compound into a blue dye product with an absorption peak at 650 nm. As shown in Fig. S11,† no absorption peaks were observed in either UMNOCC-PEG or UMNOCC-PEG + BSA groups at pH 7.4, and the mixed solution remained colorless. In comparison, intense absorption peaks were observed in both UMNOCC-PEG and UMNOCC-PEG + BSA groups at pH 6.5, suggesting that the complex formed by the protein and $Cu^{2+}$ had negligible influence on CDT. As further proof, the generation of $^1O_2$ and $^{\bullet}OH$ was determined by using an ESR spectrometer. The trapping agent of 4-amino-2,2,6,6-tetramethylpiperidine (TEMP) can react with singlet oxygen to generate the 4-amino-2,2,6,6-tetramethylpiperidine-1-oxyl (TEMPO) free radical, showing three peaks with the same strength. As displayed in Fig. 3f, this indicated that UMNOCC-PEG can generate considerable singlet oxygen by energy transfer between the UCNPs and Ce6 under near-infrared light excitation. Similarly, the capture agent of 5-(diethoxyphosphoryl)-5-methyl-1-pyrroline-*n*-oxidedmpo (DMPO) can react with generated $^{\bullet}OH$, showing a 1 : 2 : 2 : 1 four-line characteristic peak. This showed that UMNOCC-PEG can generate a large number of hydroxyl radicals by catalyzing self-supplying $H_2O_2$ in the TME. Subsequently, the UMNOCC-PEG-mediated ROS generation including $^1O_2$ and $^{\bullet}OH$ in HeLa cells was studied using the ROS probe, 2,7-dichlorofluorescin diacetate (DCFH-DA), emitting green fluorescence under 488 nm excitation. In Fig. 3g, the cells showed little fluorescence in the control group, which eliminated the interference of cell self-fluorescence. Moreover, no significant green fluorescence was detected in the UMNO group, indicating insignificant ROS generation by UMNO. Remarkably, the HeLa cells incubated with $CuO_2$ and UMNOCC-PEG exhibited stronger green fluorescence than those in the control group, while the UMNOCC-PEG treated HeLa cells upon irradiation showed the

strongest green fluorescence despite the enhanced ROS generation through the combined PDT and CDT effects. Thus, UMNOCC-PEG represents a potential drug for synergistic cancer CDT/PDT therapy.

### Determination of NO and RNS generation ability

We then evaluated the $Cu^{2+}$-controlled NO-release behavior of the UMNOCC-PEG nanoplatform under different conditions (Fig. 4a). Firstly, the generation of $H_2O_2$ arising from the decomposition of $CuO_2$ was evaluated using the typical colorimetric method, through which the yellow titanium peroxide complex ($Ti(IV)O_2^{2+}$) is formed when $H_2O_2$ oxidized colorless titanium oxysulfate ($TiOSO_4$).[54] As shown in Fig. S12,† more yellow titanium peroxide complex was obtained in the presence of UMNOCC-PEG at pH 6.5. Subsequently, we measured the release of $Cu^{2+}$ to evaluate the acid-induced dissociation behavior of UMNOCC-PEG. As displayed in Fig. 4b, the release of Cu ions was up to 80% at pH 6.5, far higher than that at pH 7.4 (6.3%), indicating that $CuO_2$ has a strong ability as the acid induced the conversion to $Cu^{2+}$ and $H_2O_2$. Significantly, such a superior acidic response to the release of Cu ions can be used as a trigger for NO therapy from RSNO. In order to assess the NO generation performance of UMNOCC-PEG, the amount of NO released was precisely determined using a typical Griess assay.[55] The released amount of NO was measured though the change in the UV–vis absorption spectra at 540 nm, and the correlation between the concentrations and absorption was measured by linear regression (Fig. S13†). As revealed in Fig. 4c, NO was produced from the as-prepared samples, with a fairly robust and rapid response at different times at pH 6.5. In contrast, there was almost no NO production at pH 7.4, wherein the release of NO was caused by the rupture of the S-NO bond in UMNOCC-PEG.

Furthermore, 3-amino-4-aminomethyl-2′,7′-difluorescein, diacetate (DAF-FM DA) was employed to investigate intracellular NO, which was oxidized by NO to produce bright green fluorescence.[56,57] The HeLa cells and UMNOCC-PEG were co-incubated at different times (10, 30, 60, and 180 min). As more UMNOCC-PEG was internalized into cells over time, large amounts of NO were released. As can be seen in Fig. 4d, the confocal laser scanning microscopy (CLSM) images showed that the green fluorescence of DAF-FM DA in cells gradually enhanced, indicating the occurrence of NO generation in cells. Afterwards, the relative fluorescence intensity in the HeLa cells

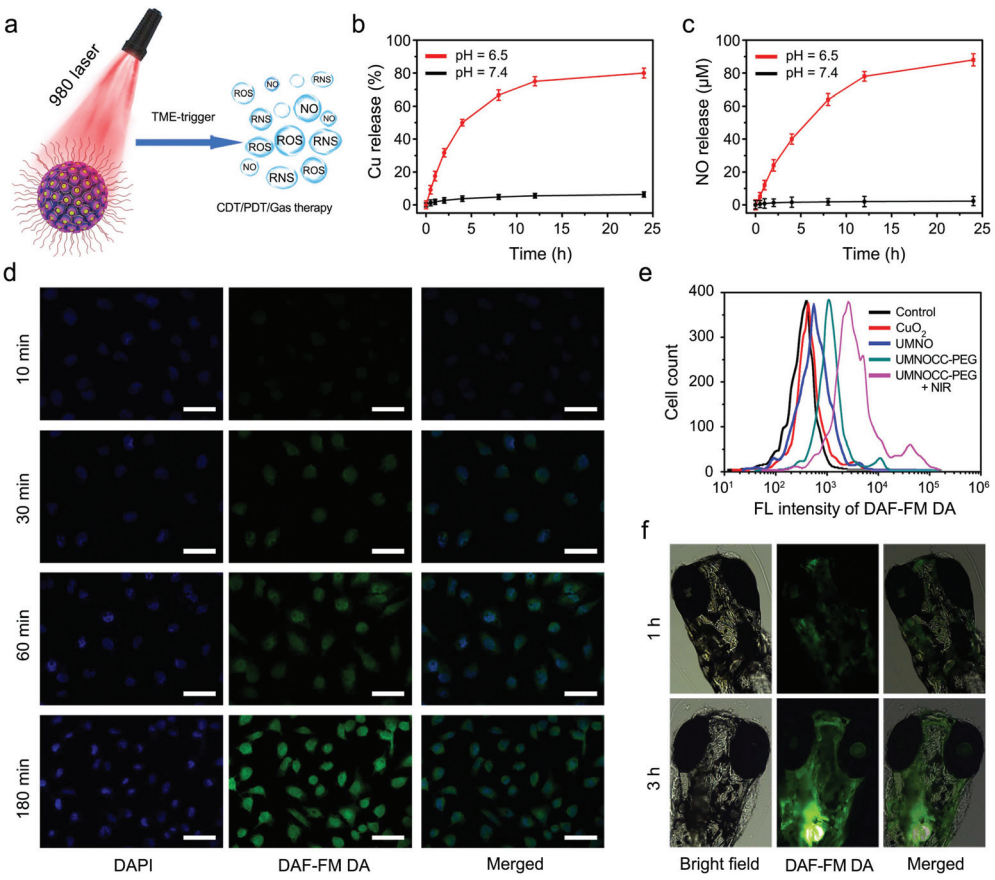


Fig. 4 Determination of NO generation ability. (a) Schematic illustration of NO release from UMNOCC-PEG. (b) Cumulative Cu release and (c) quantitative assessment of NO generation from UMNOCC-PEG under different pH conditions. (d) NO release in HeLa cells after different co-incubation times with UMNOCC-PEG. Scale bar: 50 μm. (e) Detection of intracellular NO after HeLa cells being treated with different samples by flow cytometry analyses. (f) Confocal fluorescence imaging of NO generation in living zebrafish larvae after different soaking times with UMNOCC-PEG.

was measured by flow cytometry experiments to compare the production of NO after incubation with different samples (Fig. 4e). The fluorescence intensity upon treatment with UMNOCC-PEG was visibly stronger than that of the control group, while the UMNOCC-PEG-treated HeLa cells upon irradiation show the strongest fluorescence migration, due to the production of RNS by the ROS combined with NO. Furthermore, due to the feature of optical transparency, zebrafish was employed to detect the *in vivo* NO release using a confocal fluorescence microscope. Here, zebrafish born and 3-days-old zebrafish were allowed to be soaked in the UMNOCC-PEG solution at pH 6.5. As shown in Fig. 4f, the zebrafish showed visible green signals emitted by UMNOCC-PEG treated for different times. We observed that large amounts of NO were released upon the increase of the immersion time, as evidenced by the gradually increasing green signal of NO *in vivo*. The use of peroxynitrite anions ($ONOO^-$, a major RNS), a powerful oxidizing and nitrating agent based on the reaction of ROS and NO, is an efficient cancer treatment strategy. $ONOO^-$ can oxidize dihydrorhodamine 123 (DHR) to produce rhodamine 123 (RH), showing an intensive peak at 505 nm.[58,59] As presented in Fig. S14,† there was almost no significant absorption in the UMNO group, and a powerful absorption at 505 nm was clearly observed in the UMNOCC-PEG plus NIR group, suggesting the generation of RNS. Subsequently, the generation of $ONOO^-$ was further detected by L-tyrosine, which could be oxidized by $ONOO^-$ in the presence of $CO_2$, and the oxidized dimerization of tyrosine could be measured at 406 nm upon excitation at 313 nm. As shown in Fig. S15,† the NIR group and the UMNOCC-PEG group showed almost no fluorescence signal. In contrast, the fluorescence intensity of the UMNOCC-PEG plus NIR group was significantly enhanced at 406 nm, indicating the production of abundant $ONOO^-$. These results indicate that UMNOCC-PEG was capable of producing NO and RNS molecules in the tumor microenvironment.

### Imaging performance of UMNOCC-PEG

With high spatial resolution, deep tissue penetration, and low cost, X-ray computed tomography (CT) is one of the most commonly used non-invasive imaging techniques in the clinic for cancer diagnosis.[60] The heavy rare earth ions indicate the potential applications of UMNOCC-PEG in X-ray CT imaging. The CT signals obviously enhanced as the concentration of UMNOCC-PEG increased, and the CT values had a positive linear correlation with the nanoparticle concentrations, which was attributed to the high atomic number (Z) of Gd and Yb elements (Fig. 5a and b). Subsequently, the *in vivo* CT imaging properties of UMNOCC-PEG were further assessed by the injection of nanoparticles *in situ*. In Fig. 5c and d, the tumor site had a relatively high CT value (360.6 HU), which was significantly stronger than that of the tumor site without injection (20.3 HU). Fig. 5e–f show the CT value of the tumor site in cross section and the administration group obviously fluctuated compared with the control group.

It is universally acknowledged that $Gd^{3+}$-doped nanoparticles can show a positive enhancement toward the $T_1$ signal, thus, we conclude that UMNOCC-PEG may have an excellent contrast agent of MRI.[61] As shown in Fig. 5g and h, the $T_1$ MRI signal positively enhanced with an increase of the UMNOCC-PEG concentration, and the longitudinal relaxivity ($r_1$) value was 0.9849 $mM^{-1}$ $s^{-1}$. Subsequently, we further investigated the *in vivo* MRI imaging performance of UMNOCC-PEG. As displayed in Fig. S16,† a significant $T_1$ MRI signal was observed at the tumor site after *in situ* injection. In addition, we investigated the MRI of the tumor sites after the intravenous injection of UMNOCC-PEG. As displayed in Fig. 5i, the $T_1$ MRI results showed that the significant signal enhancement occurred in the tumor tissue after UMNOCC-PEG treatment at different time points. Notably, at 12 h after the injection, the signal strength of the tumor tissue was about four times that of the non-injected one owing to the superior enhanced permeability and retention (EPR) performance of UMNOCC-PEG. These results indicate that UMNOCC-PEG may serve as an excellent MRI contrast agent. Fig. S17† displays the upconversion luminescent microscopy (UCLM) images of the HeLa cells incubated with UMNOCC-PEG for 0.5 and 1 h at 37 °C. The green luminescence of $Er^{3+}$ increased significantly with time under NIR laser irradiation. Furthermore, all the fluorescent signals were observed in intracellular regions, suggesting that UMNOCC-PEG has been endocytosed into the cells instead of merely adhering to the cell surface. On the basis of these results, we consider that UMNOCC-PEG combined with UCL/MRI/CT has better imaging performance and is a promising candidate for drug therapy.

### *In vitro* synergistic therapy of UMNOCC-PEG

Encouraged by the synergistic anticancer performance and "on-demand" NO release, a series of tests was conducted to investigate the *in vitro* anticancer properties of UMNOCC-PEG against the HeLa cell line. Once UMNOCC-PEG was ingested by tumor cells, the release of copper ions from TME-responsive $CuO_2$ will accelerate the release of NO from donors, resulting in efficient CDT therapy, and further desirable photodynamic therapy under NIR irradiation. The cellular uptake behavior of UMNOCC-PEG was researched by CLSM. Fig. S18† shows that the intracellular green fluorescence was time dependent, suggesting that fluorescein isothiocyanate (FITC)-modified UMNOCC-PEG could be effectively uptaken by the HeLa cells, and the results of ICP-MS also proved this conclusion (Fig. S19†). Moreover, the biocompatibility of UMNOCC-PEG to normal cells was investigated using L929 fibroblast cells. As displayed in Fig. 6a, the cell viability was as high as 90% even at a maximum sample concentration of 500 μg $mL^{-1}$, indicating the low cytotoxicity of UMNOCC-PEG. Subsequently, the synergetic killing efficacy of UMNOCC-PEG was evaluated by the following treatments: (1) NIR, (2) UMNO, (3) $CuO_2$, (4) UMNOCC-PEG, and (5) UMNOCC-PEG + NIR (Fig. 6b). In NIR groups, the survival rate of the cells was not reduced when treated with NIR light alone, indicating that the NIR light was harmless to the cells. The cells showed slightly decreased via-

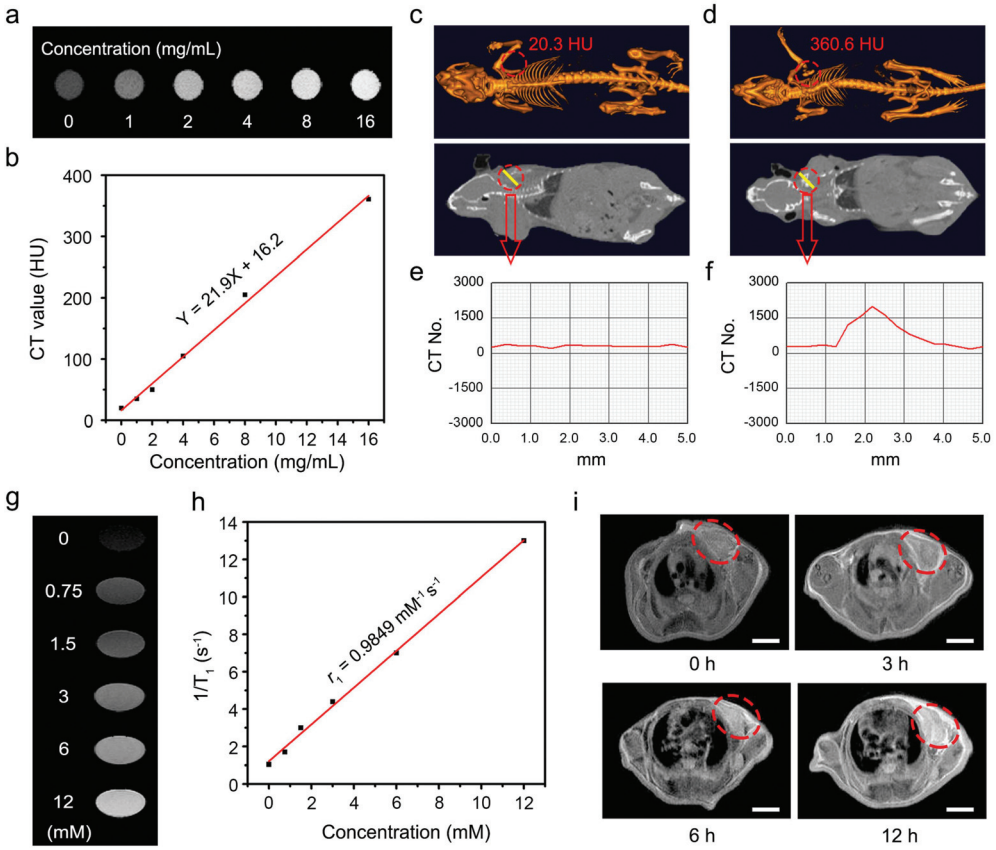


**Fig. 5** Imaging performance of UMNOCC-PEG. (a) *In vitro* CT images of UMNOCC-PEG at different concentrations and (b) corresponding CT values *versus* sample concentrations. *In vivo* CT images of tumor-bearing mice (c) before and (d) after injection and (e and f) the CT signal value of the corresponding cross section. (g) *In vitro* $T_1$-weighted MRI of UMNOCC-PEG and (h) corresponding relaxation rate $r_1$ *versus* sample concentrations. (i) $T_1$-Weighted MRI of the tumor before and after the intravenous injection of UMNOCC-PEG at different times (tumors highlighted by red circles). Scale bar: 5 mm.

bility in the UMNO and $CuO_2$ groups, which was caused by the NO induced gas therapy and single CDT effect, respectively. After incubation with UMNOCC-PEG, the anticancer effect enhanced obviously as the concentration of the sample increased, which may be assigned to the cell apoptosis induced by abundant $CuO_2$ and NO molecules. Thereafter, the survival rate of the HeLa cells treated with UMNOCC-PEG plus the NIR laser was significantly decreased to 6.4%, suggesting that the synergistic CDT/PDT/gas therapy could be achieved by UMNOCC-PEG under illumination.

As we know NO could not only relieve hypoxia by relaxing smooth muscle cells, but also react with ROS to generate the reactive nitrogen species (RNS), which can result in DNA damage and lipid peroxidation. To further investigate the performance of producing RNS from UMNOCC-PEG, phosphohistone $H_2AX$ ($\gamma$-$H_2AX$), a maker of DNA double-strand damage, was used to detect the DNA damage. Therefore, the expression of $\gamma$-$H_2AX$ in cells was subsequently confirmed by immunofluorescence staining. In Fig. 6c, the cells treated with UMNOCC-PEG plus the NIR laser exhibited the obvious fluorescence signals of $\gamma$-$H_2AX$ inside the cell nuclei compared to the control group, which suggested the augment of DNA damage by UMNOCC-PEG + NIR. Then, Calcien-AM and propidium iodide were used as fluorescent probes to confirm the cell killing efficiency after treatment. As can be seen in Fig. 6d, no significant dead cells were detected in the control group. In the UMNO, $CuO_2$, and UMNOCC-PEG groups, only a small number of red cells were clearly observed. Notably, in the UMNOCC-PEG plus NIR group, nearly all of the cells were dead, indicating the potential of the highly effective synergistic anticancer effect. Furthermore, similar therapeutic results were obtained by flow cytometry (Fig. 6e). The UMNOCC-PEG plus NIR group exhibited noticeable cell apoptosis (93.4%, early apoptosis plus late apoptosis) compared with other treatment groups. These results confirm that UMNOCC-PEG can effectively induce apoptosis though the synergistic CDT/PDT/gas therapy.

### *In vivo* synergistic therapy of UMNOCC-PEG

Based on the above experimental results, the mouse experiments using U14 tumor xenografts were conducted to explore the *in vivo* antitumor efficacy of UMNOCC-PEG. Before the anticancer therapy *in vivo*, the biological behavior of UMNOCC-PEG, including blood circulation and tissue distri-

 

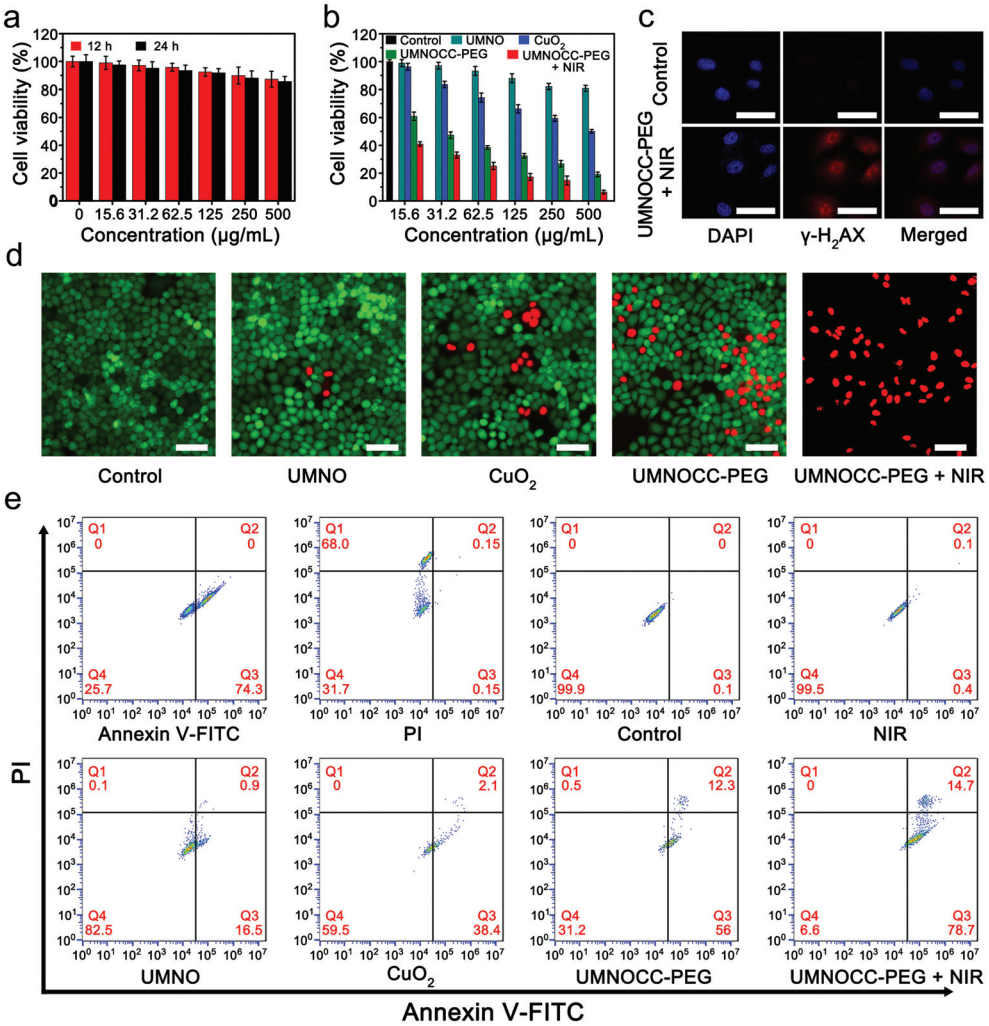


**Fig. 6** *In vitro* synergistic therapy. (a) The cell viabilities of L929 fibroblast cells upon incubation with UMNOCC-PEG for 12 h and 24 h. (b) The cell viabilities of HeLa cells after being treated under different conditions. (c) γ-$H_2AX$-stained HeLa cells treated with PBS and UMNOCC-PEG (0.5 W $cm^{-2}$, 500 μg $mL^{-1}$). Scale bar: 50 μm. (d) CLSM images of HeLa cells co-stained with calcein AM (live cells, green) and propidium iodide (dead cells, red) after being treated under different conditions (0.5 W $cm^{-2}$, 500 μg $mL^{-1}$). Scale bar: 50 μm. (e) Flow cytometry analysis of apoptosis in HeLa cells after different treatments (0.5 W $cm^{-2}$, 500 μg $mL^{-1}$).

bution, was fully evaluated by the intravenous injection of samples at different time points in tumor-bearing mice, and Cu levels in major organs and tumor tissues were detected by ICP-MS. As demonstrated in Fig. 7a, the pharmacokinetics was systematically evaluated by intravenous injection. UMNOCC-PEG exhibited a relatively long lifetime (1.3 h) in the blood, which may be due to the unique dendritic structure, uniformly nanoscale size, and excellent dispersibility of UMNOCC-PEG. Their accumulation at the tumor site was then assessed intravenously. As shown in Fig. S20,† UMNOCC-PEG could accumulate effectively at the tumor site over time through the typical EPR effect. Based on their effective accumulation at the tumor site, UMNOCC-PEG, which served as carriers of the NO donor and a copper source, could effectively deliver the NO donor to the tumor site and improve the content of $Cu^{2+}$, thus enhancing the therapeutic effect of CDT and gas therapy, while greatly reducing the side effects caused by excessive copper through the unique dendritic porous structure.

Thereafter, *in vivo* treatment experiments were conducted using U14 tumor-bearing Kunming mice, which were randomly allocated into 5 groups: (1) PBS control group, (2) UMNO, (3) $CuO_2$, (4) UMNOCC-PEG, and (5) UMNOCC-PEG + NIR. Three treatments were given intravenously at a dosage of 20 mg $kg^{-1}$ on days 0, 3, and 5 when the average tumor volume reached 100 $mm^3$. At 12 h after the intravenous injection, the irradiation groups were exposed to a 980 nm NIR laser for 10 min (0.5 W $cm^{-2}$). The tumor volumes and body weights were measured every 2 days. As shown in Fig. 7b, no abnormal weight fluctuation was observed in all groups during 20 days of treatment, suggesting negligible side-effects on the health of the mice. Then, the corresponding tumor-growth

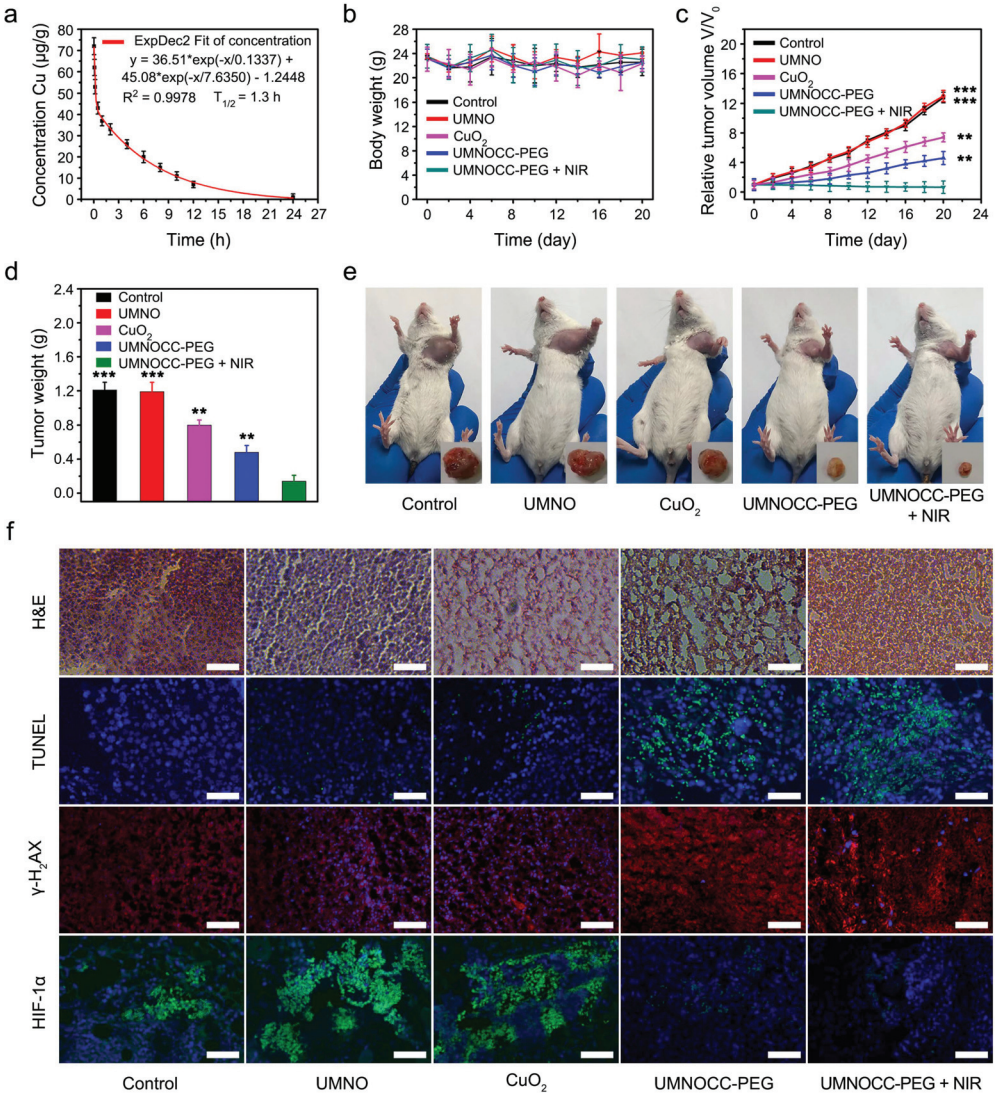


**Fig. 7** *In vivo* synergistic therapy. (a) The blood circulation in U14 tumor-bearing mice after the injection of UMNOCC-PEG intravenously. (b) Time-dependent body-weight curves and (c) changes in the relative tumor volume ($n$ = 5, mean ± SD). (d) Tumor weights of the mice after treatment for 20 days ($n$ = 5, mean ± SD). (e) Photographs of the representative mice and excised tumors. (f) H&E and TUNEL stained images and immunofluorescence analysis of tumor tissues obtained after 20 days of therapy. Scale bar: 50 μm. $^{**}P < 0.01$, $^{***}P < 0.001$.

curves are shown in Fig. 7c. Both PBS and UMNO groups showed rapid tumor growth, indicating a negligible inhibition effect. The groups treated with $CuO_2$ showed a moderate inhibitory effect, which was attributed to single CDT. In contrast, the groups treated with UMNOCC-PEG had a significant inhibitory effect on the tumor growth, and the UMNOCC-PEG injection combined with NIR irradiation results in the highest tumor inhabitation efficiency, suggesting that the combination of CDT, PDT and gas therapy exerted a highly effective synergistic anticancer effect. The mean weight of the tumors is displayed in Fig. 7d, indicating the capability of the samples to regress tumors. Subsequently, the images of the mice and the corresponding resected tumors in Fig. 7e further indicated that the tumor size in the UMNOCC-PEG plus NIR treated group was obviously smaller than those in the other groups. In addition, all mice in the UMNOCC-PEG + NIR group survived for more than 40 days, which was obviously longer than those of the other groups (Fig. S21†). Thereafter, the therapeutic efficacy was further investigated by hematoxylin and eosin (H&E) staining which demonstrated extensive tumor cell death after treatment with the UMNOCC-PEG plus NIR treated group (Fig. 7f). In contrast, the other five groups displayed little or no injury to the tumor cells, suggesting an insufficient anticancer effect. Subsequently, to further investigate the applicability of UMNOCC-PEG *in vivo*, the histopathological analysis of the main organ (heart, liver, spleen, lung and kidney) sections is shown in Fig. S22.† No obvious organ injury and pathological change were observed after various treatments, indicating no significant toxicity of the as-synthesized samples. In addition, the blood biochemical index levels of the

 

mouse treated with UMNOCC-PEG plus NIR remained normal, suggesting healthy kidney and liver functions (Fig. S23†). Subsequently, tumor tissue apoptosis was studied by the terminal deoxynucleotidyl transferase-mediated dUTP nick-end labeling (TUNEL) assay (Fig. 7f). The tumor cell apoptosis levels were enhanced in the treatment group compared with those in the saline group, indicating the excellent histological apoptosis ability of UMNOCC-PEG *in vivo*. To further investigate the levels of DNA damage and HIF-1α, the tumor sections in each group were analyzed using immunofluorescence experiments (Fig. 7f). The results showed more DNA damage in the UMNOCC-PEG plus NIR treated group than that in the other treated groups. Then, we preliminarily studied the expression of HIF-1α in tumor tissues, and the tumor sections showed a significant negative signal of HIF-1α, confirming that the tumor hypoxia state was significantly relieved, which was beneficial for improving the efficiency of PDT. Therefore, the UCL/MRI/CT trimodal imaging monitored CDT/PDT/gas therapy by UMNOCC-PEG with highly effective tumor inhibition ability and good biocompatibility was promising in cancer diagnostics and therapeutics.

# Experimental

### Chemicals

Oleic acid (OA), $ErCl_3{\cdot}6H_2O$, $YbCl_3{\cdot}6H_2O$, $GdCl_3{\cdot}6H_2O$, 1-octadecene (ODE), 3-mercaptopropyltrimethoxysilane (MPTES), poly(vinylpyrrolidone) (PVP, $M_w$ = 10 000) and *tert*-butyl nitrite (TBN) were obtained from Aladdin Reagent Co., Ltd. Tetraethyl orthosilicate (TEOS), hydrogen peroxide ($H_2O_2$, 30%), isopropyl alcohol and cyclohexane were obtained from Sinopharm Chemical Reagents Co., Ltd. copper(II) chloride dihydrate ($CuCl_2{\cdot}2H_2O$), ammonium nitrate ($NH_4NO_3$), cetyltrimethyl ammonium bromide (CTAB), sodium hydroxide (NaOH) and ammonium fluoride ($NH_4F$) were obtained from Tianjin Guangfu Reagent Co., Ltd. The apoptosis kit with annexin V-FITC and PI was obtained from Hangzhou Multi Sciences Reagent Co., Ltd. The HeLa cell line and U14 cell line were received from FDCC (Ruilu in Shanghai, China).

### Synthesis of $NaGdF_4$:Yb,Er (UCNPs)

OA-capped $NaGdF_4$:Yb,Er nanoparticles were synthesized *via* our reported method.[62] Typically, 2 mL aqueous solution of 0.4 mmol $YbCl_3{\cdot}6H_2O$, 0.04 mmol $ErCl_3{\cdot}6H_2O$, and 1.56 mmol $GdCl_3{\cdot}6H_2O$ was added into a three-necked flask containing ODE (30 mL) and OA (12 mL). The mixture was stirred evenly at room temperature for 1 h to distribute rare earth chlorides uniformly. To obtain the pale yellow precursor solution, the mixture was heated to 156 °C under slow stirring and kept for 40 min, and then cooled down to room temperature. Subsequently, $NH_4F$ (0.2964 g) and NaOH (0.2 g) were dissolved in methanol solution (10 mL) and added into the system, and then stirred for 30 min at 50 °C to evaporate methanol. The solution was heated to 110 °C and degassed for 0.5 h to maintain the system vacuum. Subsequently, the mixture was heated to 310 °C in a nitrogen atmosphere for 1.5 h and cooled naturally to 25 °C. Finally, the products were collected and washed with ethanol and cyclohexane three times.

### Synthesis of UCNP@dendritic mesoporous silica (UCNPs@dMSN)

Briefly, the above UCNP nanoparticles (10 mg) were mixed with 15 mL of cyclohexane containing isopropanol (0.5 mL) and TEOS (0.25 mL) under stirring for 10 min. Then 15 mL of water containing CTAB (0.5 g) and urea (0.3 g) was added into the above solution. The mixture was mechanically stirred for 0.5 h, and then kept at 70 °C for 16 h. Subsequently, the mixed solution was washed with ethanol several times. In order to remove the CTAB template, the above mixture was mixed with an ethanol solution (50 mL) containing 0.5 g of $NH_4NO_3$, and then kept at 65 °C for 24 h. Lastly, UCNPs@dMSN was extracted with ethanol three times.

### Synthesis of UCNPs@dMSN-SNO (UMNO)

In order to graft s-nitrosothiol (RSNO) groups to the dendritic mesoporous silica network, UCNPs@dMSN was first modified with a mercapto silane coupling agent and then reacted with *tert*-butyl nitrite. MPTES (63 μL) and ammonia (83 μL) were added into 15 mL of ethanol containing 5 mg of UCNPs@dMSN and the whole reaction system was stirred overnight. Then, the resulting UCNPs@dMSN-SH was washed with anhydrous ethanol two times and dissolved in 12.5 mL of methanol/toluene solution (v/v = 4/1). After adding 833 μL of *tert*-butyl nitrite and stirring for a day in the dark, the mixture was collected and washed with water several times to obtain UMNO.

### Synthesis of PVP-coated copper peroxide nanodots

PVP (1 g) was mixed with deionized water (10 mL) containing $CuCl_2{\cdot}2H_2O$ (0.0171 g) under ultrasonication. Subsequently, 10 mL of deionized water containing NaOH (0.008 g) was mixed with the above solution to form a green solution. Then $H_2O_2$ (100 μL) was added to the system and stirred for 30 min. The resulting products were obtained by ultrafiltration and washed three times.

### Synthesis of UCNPs@dMSN-SNO@$CuO_2$-Ce6-PEG

20 mg of copper peroxide nanodots were mixed with deionized water (8 mL) containing UCNPs@dMSN-SNO (10 mg) and the system was continuously stirred overnight. Then the mixture was washed with deionized water several times. Subsequently, 2 mL of acetone solution of Ce6 (1 mg $mL^{-1}$) was mixed with an ethanol solution (10 mL) of UCNPs@dMSN-SNO@$CuO_2$ (0.5 mg $mL^{-1}$). After sonication for 10 min, the mixture was stirred mildly for 12 h in the dark. Ultimately, the products were collected, and washed with ethanol three times. The adsorption of Ce6 to the nanoparticles was quantified by detecting the absorbance of the supernatant solution at 660 nm. Subsequently, 10 mL of the UCNPs@dMSN-SNO@$CuO_2$-Ce6 ethanol solution was mixed

with mPEG-COOH (5 mg) and stirred overnight. Then the products were washed with deionized water several times to obtain UMNOCC-PEG.

### Characterization

TEM images were acquired using a FEI Tecnai T20 transmission electron microscope. A Rigaku DMAX-2400 X-ray diffractometer equipped with a Cu Ka1 radiation source was used to characterize the X-ray diffraction (XRD) patterns. Zeta potentials and the average size of various samples were recorded by using a Zetasizer Nano ZSP. The UV-vis absorbance was obtained using a UV-1901 spectrophotometer. Confocal laser scanning microscopy (CLSM) images were obtained using a Leica TCS SP8 microscope. The ESR spectra were measured using a Bruker EMX1599 spectrometer.

### pH-responsive decomposition from UMNOCC-PEG

The acid induced dissociation of copper peroxide nanodots from UMNOCC-PEG nanoparticles was evaluated by ICP-MS. Briefly, UMNOCC-PEG (40 mg) was dissolved in 40 mL of buffer solutions (pH = 7.4 and 6.5). Subsequently, the testing solutions were placed on a constant temperature oscillator and shaked gently at 37 °C. To evaluate the release of copper ions, 2 mL of the centrifuged supernatant was extracted from each sample at given times.

### $H_2O_2$ release assay

UMNOCC-PEG (100 μg $mL^{-1}$) was added into the acetate buffer solution (pH 6.5) containing $TiOSO_4$ (30 mol $mL^{-1}$). The production of $H_2O_2$ was evaluated by the absorption increase at 405 nm. The $TiOSO_4$ solution alone was used as the control group.

### *In vitro* measurement of NO release

The NO release behavior from the nanoparticles was quantitatively examined by a typical Griess assay. The released NO molecules could react with aqueous solutions to easily become nitrates or nitrites, and then combined with the Griess agent to generate a pink diazo compound, which could be determined at 540 nm. DAF-FM DA was employed to assess the intracellular NO levels. HeLa cells were seeded in 6-well plates ($10^5$ per well) and incubated at 37 °C for 12 h. Afterward, the cells were incubated with DAF-FM DA (1 mL, 50 μM) for 30 min, the addition of 1 mL of the sample (100 μg $mL^{-1}$) and co-incubation for 3 h, then stained with DAPI (20 μg $mL^{-1}$) for 5 min. The CLSM images of released NO were obtained using a Leica TCS SP8 laser confocal microscope.

### Detection of ROS

DPBF was used to detect the generation of $^1O_2$ by UMNOCC-PEG. Typically, UMNOCC-PEG (1 mg) and DPBF (1 mg) were added into the dimethylsulfoxide solution (1 mL). Subsequently, the mixture was exposed to an NIR laser for various time periods (0, 1, 3, 5, 7 and 10 min) in the dark, and another group was not irradiated by using a 980 nm NIR laser as control. Finally, 50 μL of the supernatant was extracted and diluted to 3 mL to detect the absorbance change at 420 nm. Similarly, the generation of extracellular of hydroxyl radicals was detected by using a methylene blue probe. Briefly, UMNOCC-PEG (5 mg) and GSH (1 mM) were dispersed in PBS (pH = 7.4 and 6.5) containing methylene blue (0.01 μg $mL^{-1}$). The supernatant was collected to detect the absorbance change at 664 nm. In addition, the intracellular ROS production in HeLa cells was assessed by using the DCFH-DA chemical probe. Typically, HeLa cells were seeded in culture dishes ($10^5$ per well) and incubated at 37 °C overnight. UMNO, $CuO_2$, and UMNOCC-PEG (1 mL, 100 μg $mL^{-1}$) were added to the wells and incubated for another 3 h. Then, the cells were dyed with DCFH-DA and irradiated using the NIR laser (0.5 W $cm^{-2}$). Ultimately, the intracellular ROS images were obtained by using a CLSM.

### *In vitro* and *in vivo* MRI

250 μL of the PBS solution containing the samples of different concentrations (Gd: 0, 0.75, 1.5, 3, 6 and 12 mM) was placed on a Bruker 9.4 T MRI magnet to detect the corresponding relaxation time. Ultimately, the $r_1$ relaxivity values were obtained through fitting the curve of the $1/T_1$ relaxation time ($s^{-1}$) *versus* Gd concentration. For *in vivo* MRI, the tumor-bearing mice injected intravenously (100 μL, 1 mg $mL^{-1}$) at various time periods were anesthetized and placed on the MRI instrument, and another group without medication as a control was employed.

### CT imaging test

The CT imaging properties of UMNOCC-PEG were investigated by using a computed X-ray tomography scanner. The different concentrations of the samples were added into a 2 mL centrifuge tube for the *in vitro* CT imaging test. Subsequently, the tumor-bearing mice injected *in situ* (100 μL, 1 mg $mL^{-1}$) were anesthetized with isoflurane gas and placed on a CT scanner, and another group without medication as a control was employed.

### *In vitro* cellular uptake and UCL imaging of UMNOCC-PEG

HeLa cells were seeded in 6-well plates ($10^5$ per well) and incubated overnight at 37 °C. UMNOCC-PEG (100 μg $mL^{-1}$) was added into wells and incubated for different times. Thereafter, the DAPI solution (1 mL, 20 μg $mL^{-1}$) was used to stain the nucleus. Finally, the cellular uptake images were obtained by CLSM. For the UCL imaging of UMNOCC-PEG, the experimental procedure is the same except that the cells were excited by using NIR light and observed by using an inverted fluorescence microscope.

### *In vitro* cytotoxicity

Typically, HeLa cells were seeded in 96-well plates ($10^4$ per well) and incubated overnight at 37 °C to form adherent cells. Subsequently, UMNO, $CuO_2$, and UMNOCC-PEG were added to the wells at different concentrations, respectively. The concentration of $CuO_2$ was in accordance with that of $CuO_2$ in UMNOCC-PEG. After 4 h of cultivation, the cells in the light group were irradiated with an NIR laser for 10 min. Then the

 

cells were incubated for another 24 h. Thereafter, 20 μL of MTT (5 mg $mL^{-1}$) was added to each well and incubated at 37 °C for another 4 h. Ultimately, 150 μL of DMSO was added to each well and the absorbance at 490 nm was measured by using an enzyme standard instrument. A similar MTT assay was used to determine the *in vitro* viability of UMNOCC-PEG to L929 cells, and the concentrations of the materials were 0, 15.6, 31.2, 62.5, 125, 250, and 500 μg $mL^{-1}$.

### Analysis of apoptosis

HeLa cells were seeded in 6-well plates ($10^5$ per well) and incubated overnight at 37 °C to form adherent cells. Subsequently, the cells were treated with different samples and incubated for 24 h. Finally, 5 μL of Annexin V-FITC and 10 μL of PI were added to each tube and incubated at 25 °C in the dark for 5 min. Cancer cell apoptosis was detected by using a BD Accuri C6 flow cytometer.

### Animal experiment

Kunming mice (8 weeks, female) were purchased from Second Affiliated Hospital, Harbin Medical University. All the animal experiments were performed in strict accordance with The National Regulation of China for Care and Use of Laboratory Animals issued by the State Science and Technology Commission (no. 676 Rev. 2017), and have been approved by the Ethics Committee of the Second Affiliated Hospital of Harbin Medical University. The ethical review number is SYDW 2019–82.

### Blood circulation and biodistribution of UMNOCC-PEG

Briefly, 20 μL of blood samples were collected at various time periods after the intravenous injection of UMNOCC-PEG (100 μL, 4 mg $mL^{-1}$). The circulation time in the bloodstream was evaluated by detecting the Gd concentration. For *in vivo* biodistribution, U14 cancer cells were subcutaneously injected to the left axilla of all the mice. When the tumor volume increases to about 100 $mm^3$, the distribution of the sample was assessed by the intravenous injection of UMNOCC-PEG (100 μL, 20 mg $kg^{-1}$) into the mice ($n$ = 3). Soon afterward, the main organs (heart, liver, spleen, lung, and kidney) and tumors were collected at different time points (0.5, 1, 4, 12, 24, and 48 h). Finally, the Cu concentration was measured by ICP-MS.

### *In vivo* evaluation of synergistic CDT/PDT/gas therapy

The mice were randomly divided into five groups ($n$ = 5). The first group of mice was injected into PBS as the control group. The other four groups were treated with UMNO, copper peroxide, and UMNOCC-PEG (10 mg $mL^{-1}$, in 150 μL PBS). The weight of the mice was recorded every 2 days. To evaluate the growth of tumor, a vernier caliper was used to measure the width and length of the tumor. The tumor volume was assessed by using the following equation: $V$ = Length × $Width^2/2$. Finally, the major organs and tumors were sliced and dyed with hematoxylin and eosin for histological analysis. Furthermore, the levels of DNA damage and the hypoxia inducible factor (HIF-1α) in the tumor sections of each group were analyzed by performing immunofluorescence experiments.

## Conclusions

In summary, we successfully established a novel $Cu^{2+}$-controlled NO-release platform based on up-conversion dendritic mesoporous silica nanocomposites for multiple imaging guided synergistic CDT/PDT/gas therapies. This nanoplatform can integrate NO donors (RSNO) by engineering the UCNP surface with a dendritic mesoporous silica layer, where Ce6 and the trigger of RSNO were effectively loaded into the super large silica channel for "on-demand" $Cu^{2+}$-triggered NO generation. The accompanying Fenton-like reaction between the decomposition products generated $^{\bullet}OH$ for enhanced CDT though self-supplying $H_2O_2$. Notably, the release of NO also evidently reduces tumor hypoxia, possibly through increasing the blood flow due to smooth muscle cell relaxation, thereby successfully overcoming the limitations of PDT and significantly improving its efficiency. More importantly, the efficient RNS release could be achieved by the simultaneous generation of ROS and NO. The produced RNS can directly induce DNA damage, and significantly improve the therapeutic effect. Systematic *in vitro* and *in vivo* experiments have demonstrated that the nanocomposite exhibited effective therapeutic efficacy toward cancer cells by inducing cancer cell apoptosis. Simultaneously, the UCL/MRI/CT tri-mode imaging could be applied for guiding and monitoring the therapeutic process, achieving the accurate cancer treatment. As a result, the proposed ROS plus RNS nanoplatform not only provides a novel efficient cancer treatment modality, but also pioneers the field of copper controlled therapeutic gas production for cancer therapeutics.

## Conflicts of interest

There are no conflicts to declare.

## Acknowledgements

Financial support from the National Natural Science Foundation of China (NSFC 51972075, 51972076, and 51772059), the Natural Science Foundation of Heilongjiang Province (YQ2019E014), the Natural Science Foundation of Shandong Province (ZR2019ZD29), the Postdoctoral Scientific Research Developmental Fund (LBH-Q18034), the Ph.D. Student Research and Innovation Fund of the Fundamental Research Funds for the Central Universities (3072020GIP1016), the Open Funds of the State Key Laboratory of Rare Earth Resource Utilization (RERU2020002), and the Fundamental Research funds for the Central Universities is greatly acknowledged.

## References

1 S. Li, R. Liu, X. Jiang, Y. Qu, X. Song, G. Huang, N. Fu, L. Lin, J. Song, X. Chen and H. Yang, *ACS Nano*, 2019, **13**, 2103–2113.

2 S. B. Wang, C. Zhang, Z. X. Chen, J. J. Ye, S. Y. Peng, L. Rong, C. J. Liu and X. Z. Zhang, *ACS Nano*, 2019, **13**, 5523–5532.
3 L. Yu, P. Hu and Y. Chen, *Adv. Mater.*, 2018, **30**, 1801964.
4 W. Fan, B. C. Yung and X. Chen, *Angew. Chem., Int. Ed.*, 2018, **57**, 8383–8394.
5 X. Zhang, J. Du, Z. Guo, J. Yu, Q. Gao, W. Yin, S. Zhu, Z. Gu and Y. Zhao, *Adv. Sci.*, 2019, **6**, 1801122.
6 X. Zhang, G. Tian, W. Yin, L. Wang, X. Zheng, L. Yan, J. Li, H. Su, C. Chen, Z. Gu and Y. Zhao, *Adv. Funct. Mater.*, 2015, **25**, 3049–3056.
7 W. Fan, N. Lu, P. Huang, Y. Liu, Z. Yang, S. Wang, G. Yu, Y. Liu, J. Hu, Q. He, J. Qu, T. Wang and X. Chen, *Angew. Chem., Int. Ed.*, 2017, **56**, 1229–1233.
8 Z. Du, X. Zhang, Z. Guo, J. Xie, X. Dong, S. Zhu, J. Du, Z. Gu and Y. Zhao, *Adv. Mater.*, 2018, **30**, 1804046.
9 R. Guo, Y. Tian, Y. Wang and W. Yang, *Adv. Funct. Mater.*, 2017, **27**, 1606398.
10 H. J. Xiang, L. An, W. W. Tang, S. P. Yang and J. G. Liu, *Chem. Commun.*, 2015, **51**, 2555–2558.
11 H. J. Xiang, Q. Deng, L. An, M. Guo, S. P. Yang and J. G. Liu, *Chem. Commun.*, 2016, **52**, 148–151.
12 D. A. Riccio and M. H. Schoenfisch, *Chem. Soc. Rev.*, 2012, **41**, 3731–3741.
13 D. A. Wink, Y. Vodovotz, J. Laval, F. Laval, M. W. Dewhirst and J. B. Mitchell, *Carcinogenesis*, 1998, **19**, 711–721.
14 P. G. Wang, M. Xian, X. P. Tang, X. J. Wu, Z. Wen, T. W. Cai and A. J. Janczuk, *Chem. Rev.*, 2002, **102**, 1091–1134.
15 H. Yin, X. Guan, H. Lin, Y. Pu, Y. Fang, W. Yue, B. Zhou, Q. Wang, Y. Chen and H. Xu, *Adv. Sci.*, 2020, **7**, 1901954.
16 K. Zhang, H. Xu, X. Jia, Y. Chen, M. Ma, L. Sun and H. Chen, *ACS Nano*, 2016, **10**, 10816–10828.
17 W. Fan, W. Bu, Z. Zhang, B. Shen, H. Zhang, Q. He, D. Ni, Z. Cui, K. Zhao, J. Bu, J. Du, J. Liu and J. Shi, *Angew. Chem., Int. Ed.*, 2015, **54**, 14026–14030.
18 J. Li, R. Jiang, Q. Wang, X. Li, X. Hu, Y. Yuan, X. Lu, W. Wang, W. Huang and Q. Fan, *Biomaterials*, 2019, **217**, 119304.
19 S. Dong, J. Xu, T. Jia, M. Xu, C. Zhong, G. Yang, J. Li, D. Yang, F. He, S. Gai, P. Yang and J. Lin, *Chem. Sci.*, 2019, **10**, 4259–4271.
20 C. Liu, B. Liu, J. Zhao, Z. Di, D. Chen, Z. Gu, L. Li and Y. Zhao, *Angew. Chem., Int. Ed.*, 2020, **59**, 2634–2638.
21 Y. Liu, W. Zhen, L. Jin, S. Zhang, G. Sun, T. Zhang, X. Xu, S. Song, Y. Wang, J. Liu and H. Zhang, *ACS Nano*, 2018, **12**, 4886–4893.
22 J. Xu, W. Han, P. Yang, T. Jia, S. Dong, H. Bi, A. Gulzar, D. Yang, S. Gai, F. He, J. Lin and C. Li, *Adv. Funct. Mater.*, 2018, **28**, 1803804.
23 C. Liu, D. Wang, S. Zhang, Y. Cheng, F. Yang, Y. Xing, T. Xu, H. Dong and X. Zhang, *ACS Nano*, 2019, **13**, 4267–4277.
24 G. Yang, L. Xu, J. Xu, R. Zhang, G. Song, Y. Chao, L. Feng, F. Han, Z. Dong, B. Li and Z. Liu, *Nano Lett.*, 2018, **18**, 2475–2484.
25 L. Brunet, D. Y. Lyon, E. M. Hotze, P. J. J. Alvarez and M. R. Wiesner, *Environ. Sci. Technol.*, 2009, **43**, 4355–4360.
26 X. Chen, H. Zhang, M. Zhang, P. Zhao, R. Song, T. Gong, Y. Liu, X. He, K. Zhao and W. Bu, *Adv. Funct. Mater.*, 2020, **30**, 1908365.
27 D. Slade and M. Radman, *Microbiol. Mol. Biol. Rev.*, 2011, **75**, 133–191.
28 B. Ding, S. Shao, C. Yu, B. Teng, M. Wang, Z. Cheng, K.-L. Wong, P. a. Ma and J. Lin, *Adv. Mater.*, 2018, **30**, 1802479.
29 L. Feng, S. Gai, F. He, Y. Dai, C. Zhong, P. Yang and J. Lin, *Biomaterials*, 2017, **147**, 39–52.
30 Y. Y. Liu, X. F. Meng and W. B. Bu, *Coord. Chem. Rev.*, 2019, **379**, 82–98.
31 M. Huo, L. Wang, L. Zhang, C. Wei, Y. Chen and J. Shi, *Angew. Chem., Int. Ed.*, 2020, **59**, 1906–1913.
32 Q. Jia, J. Ge, W. Liu, X. Zheng, S. Chen, Y. Wen, H. Zhang and P. Wang, *Adv. Mater.*, 2018, **30**, 1706090.
33 D. Wang, H. Wu, W. Q. Lim, S. Z. F. Phua, P. Xu, Q. Chen, Z. Guo and Y. Zhao, *Adv. Mater.*, 2019, **31**, 1901893.
34 Z. Chen, Z. Liu, Z. Li, E. Ju, N. Gao, L. Zhou, J. Ren and X. Qu, *Biomaterials*, 2015, **39**, 15–22.
35 G. Yang, L. Xu, Y. Chao, J. Xu, X. Sun, Y. Wu, R. Peng and Z. Liu, *Nat. Commun.*, 2017, **8**, 902.
36 L. J. Ignarro, G. M. Buga, K. S. Wood, R. E. Byrns and G. Chaudhuri, *Proc. Natl. Acad. Sci. U. S. A.*, 1987, **84**, 9265–9269.
37 H. Shimokawa and S. Godo, *J. Cardiovasc. Pharmacol.*, 2016, **67**, 361–366.
38 W. Wu, L. Yu, Q. Jiang, M. Huo, H. Lin, L. Wang, Y. Chen and J. Shi, *J. Am. Chem. Soc.*, 2019, **141**, 11531–11539.
39 P. Zhao, Z. Tang, X. Chen, Z. He, X. He, M. Zhang, Y. Liu, D. Ren, K. Zhao and W. Bu, *Mater. Horiz.*, 2019, **6**, 369–374.
40 C. Zhang, L. Yan, X. Wang, X. Dong, R. Zhou, Z. Gu and Y. Zhao, *Nano Lett.*, 2019, **19**, 1749–1757.
41 M. Chang, M. Wang, M. Wang, M. Shu, B. Ding, C. Li, M. Pang, S. Cui, Z. Hou and J. Lin, *Adv. Mater.*, 2019, **31**, 1905271.
42 Z. Tang, Y. Liu, M. He and W. Bu, *Angew. Chem., Int. Ed.*, 2019, **58**, 946–956.
43 H. Burachaloo, P. A. Gurr, D. E. Dunstan and G. G. Qiao, *ACS Nano*, 2018, **12**, 11819–11837.
44 Y. Han, J. Ouyang, Y. Li, F. Wang and J.-H. Jiang, *ACS Appl. Mater. Interfaces*, 2020, **12**, 288–297.
45 M. Huo, L. Wang, Y. Chen and J. Shi, *Nat. Commun.*, 2017, **8**, 357.
46 N. A. Stasko, T. H. Fischer and M. H. Schoenfisch, *Biomacromolecules*, 2008, **9**, 834–841.
47 D. A. Riccio, J. L. Nugent and M. H. Schoenfisch, *Chem. Mater.*, 2011, **23**, 1727–1735.
48 D. S. Moon and J. K. Lee, *Langmuir*, 2012, **28**, 12341–12347.
49 S. L. Gai, P. P. Yang, P. A. Ma, D. Wang, C. X. Li, X. B. Li, N. Niu and J. Lin, *J. Mater. Chem.*, 2011, **21**, 16420–16426.
50 V. Polshettiwar, D. Cha, X. X. Zhang and J. M. Basset, *Angew. Chem., Int. Ed.*, 2010, **49**, 9652–9656.
51 X. Du and J. H. He, *Nanoscale*, 2012, **4**, 852–859.
52 L. S. Lin, T. Huang, J. B. Song, X. Y. Ou, Z. T. Wang, H. Z. Deng, R. Tian, Y. J. Liu, J. F. Wang, Y. Liu, G. C. Yu, Z. J. Zhou, S. Wang, G. Niu, H. H. Yang and X. Y. Chen, *J. Am. Chem. Soc.*, 2019, **141**, 9937–9945.

53 Z. P. Wang, Y. G. Zhang, Z. C. Tan and Q. H. Li, *Chem. Eng. J.*, 2018, **350**, 767–775.
54 R. Zhang, L. Z. Feng, Z. L. Dong, L. Wang, C. Liang, J. W. Chen, Q. X. Ma, R. Zhang, Q. Chen, Y. C. Wang and Z. Liu, *Biomaterials*, 2018, **162**, 123–131.
55 J. Sun, X. J. Zhang, M. Broderick and H. Fein, *Sensors*, 2003, **3**, 276–284.
56 Q. Zhao, J. M. Zhang, L. J. Song, Q. Ji, Y. Yao, Y. Cui, J. Shen, P. G. Wang and D. L. Kong, *Biomaterials*, 2013, **34**, 8450–8458.
57 M. Liong, J. Lu, M. Kovochich, T. Xia, S. G. Ruehm, A. E. Nel, F. Tamanoi and J. I. Zink, *ACS Nano*, 2008, **2**, 889–896.
58 J. Gehring, B. Trepka, N. Klinkenberg, H. Bronner, D. Schleheck and S. Polarz, *J. Am. Chem. Soc.*, 2016, **138**, 3076–3084.
59 Y. Y. Yuan, C. J. Zhang and B. Liu, *Angew. Chem., Int. Ed.*, 2015, **54**, 11419–11423.
60 J. T. Xu, P. P. Yang, M. D. Sun, H. T. Bi, B. Liu, D. Yang, S. L. Gai, F. He and J. Lin, *ACS Nano*, 2017, **11**, 4133–4144.
61 Z. G. Yi, Z. C. Luo, N. D. Barth, X. F. Meng, H. Liu, W. B. Bu, A. All, M. Vendrell and X. G. Liu, *Adv. Mater.*, 2019, **31**, 1901851.
62 S. K. Liu, W. T. Li, S. M. Dong, S. L. Gai, Y. S. Dong, D. Yang, Y. L. Dai, F. He and P. P. Yang, *ACS Appl. Mater. Interfaces*, 2019, **11**, 47659–47670.